Chapter 4

Analytical Electron Microscopy — Study of All Solid-State Batteries

Ziying Wang and Ying Shirley Meng
Department of NanoEngineering
UC San Diego
La Jolla, CA 92093-0448, USA

This chapter focuses on the recent development and optimization of analytical electron microscopy to understand the dynamic changes in the bulk and interfaces of electrodes and electrolytes within all solid-state batteries. Three major aspects are covered: (1) design and fabrication of all solid-state batteries that remain functional after careful focused ion beam (FIB) processing; (2) enablement of *in-situ* biasing in both FIB/SEM and transmission electron microscope and/or scanning transmission electron microscope (TEM/STEM); and (3) development of the fundamental understanding of the dynamic chemical and electronic processes at the solid/solid interfaces of electrode/electrolyte by high resolution imaging and electron energy loss spectroscopy (EELS). Our goal is to apply analytical microscopy to gain new insights that can help us make significant inroads towards understanding the basic science of ion transport, charge transfer and related phase transformations in electrochemical systems at the nanometer scale.

1. Introduction

In-situ electrochemical operation in the ultra-high vacuum column of a Transmission Electron Microscopy (TEM) has been pursued by two major strategies. In one strategy, a "nano-battery" is fabricated from an all-solid-state thin film battery using a focused ion beam (FIB). The electrolyte is either polymer based or ceramic based without any liquid components. The second strategy involves liquid electrolytes.

Although the latter approach more closely resembles the actual operating conditions of the widely-used functional battery, the extreme volatility of the organic electrolytes presents a significant challenge for designing an *in-situ* cell suitable for the vacuum environment of the TEM. Ionic liquids can be used to replace the conventional polycarbonate based electrolytes without the tedious silicon nitride window sealing cell setup. More recently, it has been reported that Li_2O can be used as a low-voltage electrolyte for lithiation in Si/Sn/Ge and FeF_2 electrode materials.[1–4] However, Li_2O is unstable upon high voltage charging. Therefore, it would not be suitable for high voltage delithiation of transition metal oxides, a common class of materials used as the positive electrode in lithium-ion batteries.

Significant progress has been made in the past few years on the development of *in-situ* electron microscopy for probing nanoscale electrochemistry. Both strategies mentioned above are pursued in the research community. Yamamoto *et al.* reported the dynamic visualization of electric potential in an all solid-state battery by electron holography and electron energy loss spectroscopy (EELS).[5] They emphasized the need for thicker electrolyte while preparing the cross-section using FIB to avoid short-circuiting during the biasing process. Their experimental set up consisted of an electrolyte that was too thick (90 μm) and only a smaller portion of the cross-section was thinned down to be observed in the TEM while the whole stack was biased. In spite of the *in-situ* observation in TEM, the problem with this configuration was that the thinner part ($\sim$60 nm) observed in TEM had higher resistance than other parts of the cross-section and led to very minimal electrochemical activity. More recently, there has been tremendous progress on *in-situ* studies using Si nanowires,[1,6] Ge nanowires,[3] and SnO_2 nanowires[7,8] as anode materials. Ionic liquid was mostly used as electrolyte. A schematic of the experimental set up is shown in Fig. 1. With a similar setup, Feng *et al.*[2] successfully used Li_2O as the electrolyte and lithiated FeF_2, a conversion type electrode material. A novel "necking" phenomenon was revealed in the nano-composite materials by this *in-situ* TEM technique.

Despite the success of *in-situ* biasing experiments of individual nanowires and nanoparticles, there are several drawbacks to the
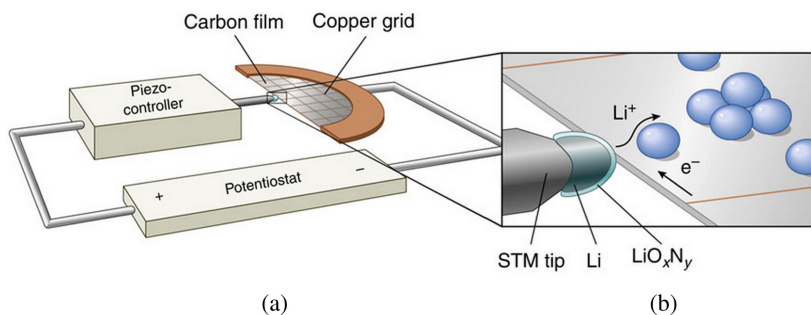
Fig. 1. From Ref. 2, (a) schematic of the electrochemical cell used for *in-situ* TEM measurements. (b) Time-lapse images from a collection of particles that react with lithium coming from the lower right. The reaction proceeds immediately in region (I), but is delayed and absent in regions (II) and (III), respectively. Scale bar, 10 nm.

approach, such as:

1. The chemistry of individual nano-materials seems to be unique and generalizing the results to an electrochemically active system is debatable (particularly when the individual and ensemble effects of nano-materials are different).
2. Ionic liquid is of low vapor pressure, and use of IL in the UHV column may induce long-term damage to the microscopes.
3. Electrode/electrolyte interface is very important in energy storage devices, which cannot be addressed directly by these studies.

Considering the above points, our approach has unique advantages because our starting point is an electrochemically active solid-state battery stack. This type of all solid-state sample can be used to study the interface effects *in-situ* while monitoring electrochemical and structural changes with high spatial resolution. We demonstrate that the FIB processed cross-section is still electrochemically active and *in-situ* TEM can be used as an advanced tool to monitor the electrode/electrolyte interface during the operation of the battery.

2. FIB Fabrication and Electrochemical Biasing of Nano-Batteries

The eventual success of *in-situ* analytical TEM depends on the fabrication of less than 100 nm thick all solid-state lithium-ion

batteries that are electrochemically active. As one of the few methods capable of such fabrication, FIB technique has been used for TEM specimen preparation and semiconductor circuit editing quite extensively.[9,10] Major concerns with FIB have been the surface damage, re-deposition, and preferential sputtering due to high current density.[11,12] Several articles on the FIB damage to materials during preparation of specimens have proposed possible methods to reduce this damage.[13–16] FIB fabrication of electrochemically functional all solid-state nano-batteries depends on two main factors: Limitation of structural damage caused by high ion beam current and avoidance of shorting caused by re-deposition during milling processes.

Using an all solid-state battery with Si, LiPON, and $LiCoO_2$ as anode, electrolyte, and cathode respectively as the typical system, functional nano-batteries have been fabricated using a two-step procedure with a specific set of beam parameters. The successful preservation of electrochemical functionality depends on several parameters; most importantly, the ion beam current and the pixel dwell time. For typical FIB fabrications, beam energy and current are given more importance compared to pixel dwell time. Here, we demonstrate that pixel dwell time to be a very important parameter. To reduce the fabrication time and damage induced by FIB, a two-step fabrication process was utilized. The first step is a high current (≤ 2.8 nA) milling process followed by a low current (0.28 nA) cross-section cleaning process while maintaining the 30 kV incident beam. During the first step high current leads to a large amount of re-deposition across the stack and the second step cleans the cross-section. Figures 2(a) and 2(b) shows the cross-section SEM images of the $Si/LIPON/LiCoO_2$ battery stack which clearly depicts the effect of this two-step fabrication process. High ion beam current (>0.28 nA) during the surface cleaning process tends to heat the amorphous electrolyte and worsen re-deposition across the stack.

The second important parameter is the pixel dwell time, defined as how long the ion beam dwells on each pixel during a scanning process. Higher dwell time also leads to heating and increasing re-deposition, causing loss of electrochemical activity of the battery stack. Figure 3 shows the effect of pixel dwell time on the
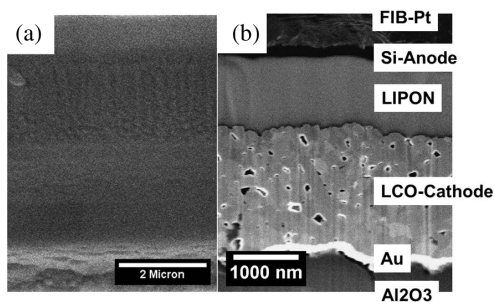
Fig. 2. SEM images of the all solid-state battery (effect of two-step fabrication process). (a) After step one: Milling process. (b) After step two: Cross-section cleaning.[17]
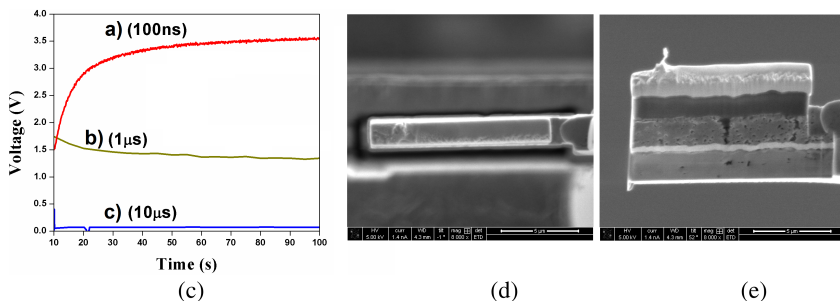

Fig. 3. Electrochemical voltage profile of all solid-state batteries fabricated by FIB. (a) 100 ns pixel dwell time, (b) 1 μs pixel dwell time, (c) 10 μs pixel dwell time. (d) and (e) show the typical dimensions of a nano-battery from top-view and side-view.[17]

electrochemical activity of a sputtered micro-battery stack fabricated by FIB. The stack was charged under constant current mode (typically with a current density of about $100 \, \mu A/cm^2$) *in-situ* in a FIB system. The normal size of the nano-batteries fabricated is a $2 \, \mu m \times 10 \, \mu m$ rectangle with the thickness of the whole battery stack.

In Fig. 3(a), the charging profile for a nano-battery fabricated using $100 \, \mu s$ pixel dwell time shows hardly any voltage, indicating shorting across the stack. Figure 3(b) shows the charging curve for a nano-battery fabricated using $1 \, \mu s$ pixel dwell time, and the voltage was lower than the expected 3.6 V. Figure 3(c) shows the charging profile for a nano-battery fabricated using 100 ns pixel dwell time and the voltage raised to 3.6 V. For all the three cases, the charging

current density was $100\,\mu A/cm^2$. Nano-batteries fabricated using 100 ns pixel dwell time are highly consistent and repeatable with 3.6 V voltage plateau which agrees well with the voltage profile of macro-batteries in literature.[18] Subsequent to the successful nano-battery fabrication, we scaled down to fabricate even thinner nano-batteries.

The specific procedures of electrochemically biasing the batteries inside the FIB are fairly simple and straight forward. A micron slab consisting of the whole battery stack is lifted out of the all solid-state thin film battery using typical TEM sample preparation procedures.[9] The liftout procedure must be conducted with the aforementioned maximum FIB current setting and pixel dwell time parameters. Once this sample is mounted on a typical OmniProbe copper grid for TEM samples via Pt-welding, a small cleaning cross-section is used to expose the whole battery stack near the welding area. Afterwards, a second Pt-welding is used to connect the previous Pt-weld (which is connected to the Cu grid) to the exposed Au-bottom current collector. This ensures an electrical connection from the FIB stage to the cathode of the nano-battery. In order to isolate the top anode Silicon layer, cleaning cross-sections are applied from a side-view to remove a portion of the battery down to the lithium cobalt oxide layer. Finally, the nano-battery is milled to the desired size by cleaning cross-sections from the top-view. The anode connection is made by physically contacting the Omniprobe micromanipulator to the top surface of the nano-battery. Most FIB models will support outside electrical connections to the stage and omniprobe via electrical ports, hence establishing electrical connections from the nano-battery to an external battery cycler. Figure 4 demonstrates the procedures involved in the fabrication and biasing of a nano-battery.

3. Beam Damage Control in TEM/STEM

After the successful fabrication of nano-batteries with careful FIB parameter control, electron beam damage under scanning transmission electron microscope (STEM) and EELS with a highly focused
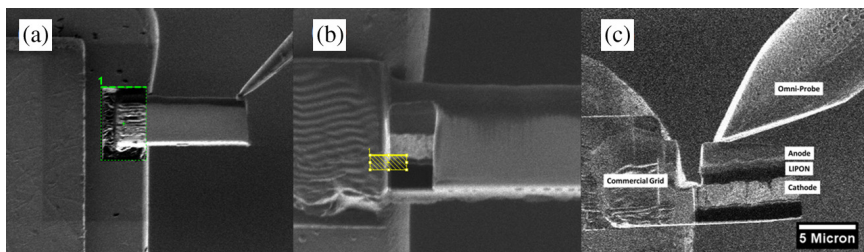
Fig. 4. (a) Mounting of nano-battery after the liftout. (b) Cleaning cross-section to expose battery layers and Pt-welding for electrical connection. (c) Electrical contact to the nano-battery after cleaning the cross-section.

electron beam must be controlled and minimized in order to extract useful analytical information. The most critical aspect related to the non-destructive lithium transport evaluation in electron microscopes is the stability of the solid-electrolyte under the intense electron beams. Current densities in modern STEM imaging and EELS have increased significantly due to high focusing capabilities of the modern microscopes, leading to e-beam damage of nano-materials.[19–22] Materials, depending on their physical and thermal properties respond to e-beam dosage in different ways with threshold doses for damage-less imaging. E-beam dose is calculated by multiplying the current density and the exposure time in each pixel and indicated by the number of electrons/nm^2. Threshold doses reported in literature vary from as small as 5×10^2 e$^-$/nm^2 for 100 keV incident energy of the electrons to about 10^7 e$^-$/nm^2 for 200 keV.[20–23] The contributing factors for the e-beam induced damages are: (i) atomic displacements, (ii) e-beam sputtering, (iii) e-beam heating, (iv) electro-static charging, and (v) radiolysis.[19] At high incident energies, most of the energy lost by the electrons is due to inelastic scattering which can eventually heat up the sample locally if the thermal conductivity of the sample is low.[19] For electrically-insulating samples at high current densities, lateral migration of ions is possible due to electrostatic charging induced electric fields across the samples.[19] Similarly, radiolysis (e-beam degradation) induced mass loss is also possible. For example, fluorine loss in AlF$_3$ and metallic Al-nanoparticle formation has

been observed due to radiolysis.[19] Lithium phosphorous oxynitride (LIPON) is amorphous, electronically non-conducting and has low thermal conductivity. LIPON is a commercialized solid electrolyte and has been used in all solid-state batteries for a long time now.[24,25] Among the above-mentioned aspects of damage, e-beam heating, electrostatic charging and radiolysis are all relevant for this work considering the physical, electrical and thermal properties of the solid electrolyte LIPON. In this chapter, we report the stability of LIPON under both high flux electron and ion beams and present how the beam induced instability can affect the functionality of the nano-batteries and quantitative analysis of EELS data. This type of analysis must be conducted for any solid electrolyte since they are intrinsically susceptible to beam damage.

LIPON is highly sensitive to both e-beam and ion beam damage. Large electron dose leads to decomposition of the electrolyte which is not desirable for the functionality of the battery. The mechanism of LIPON damage can be attributed to three factors (i) electrostatic charging, (ii) beam heating and (iii) radiolysis. Figure 5 shows the STEM images recorded after EELS mapping in the region indicated
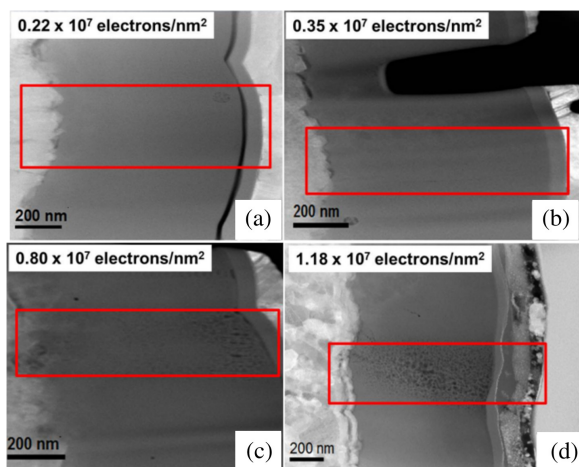

Fig. 5. Electron dose effect on LiPON during STEM/EELS mapping at various dosage. (a) and (b) show no observable damage while (c) and (d) show formation of voids in LiPON.[17]

by the box in each image. Figures 5(a) and 5(b) show that the LIPON is undamaged while 5(c) and 5(d) show that the LIPON is damaged as seen by the dark contrast in most of the pixels. The legends in each figure indicate the electron dose used for EELS mapping which clearly shows that there is a threshold dose of about $0.5 \times 10^7 \, e^-/nm^2$, below which no damage can be observed. Both the cathode and anode have very high threshold and do not show any damage at this dose level. These are representative images from many observations and irrespective of pixel size and dwell time. Beyond the threshold dose, damage can be observed.

This damage also manifests significant changes in the EELS spectrum edge of elements, more specifically on the Li K-edge. The damaged region shows lower intensity for Li K-edge (as shown in Fig. 6 and the inset) for the spectra collected from the same sample but with different electron doses. The lower intensity of lithium
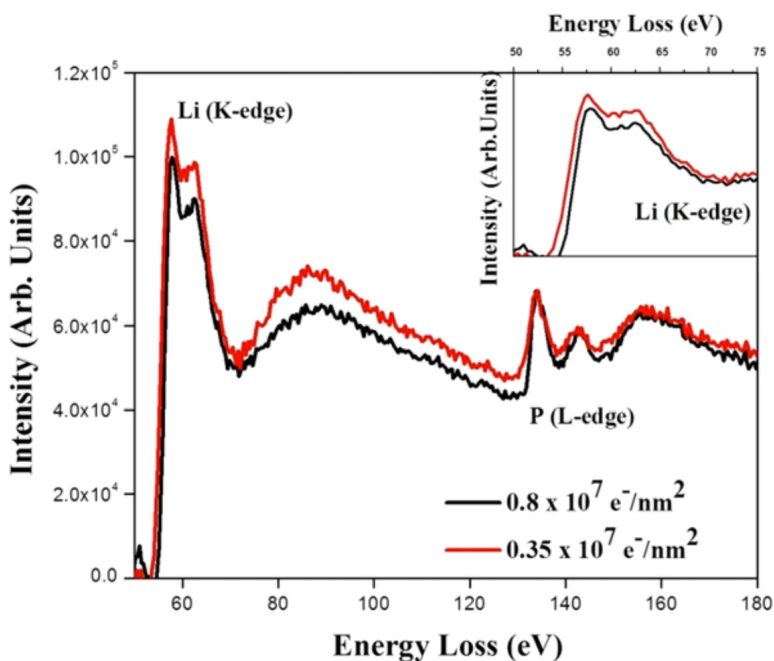

Fig. 6. Electron dose effect on EELS signal of Li-edge. Larger dose not only damages the LIPON, but also decreases the Li signal intensity.
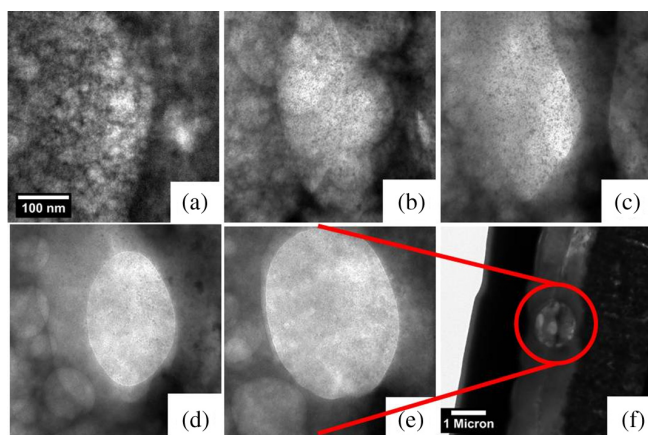
Fig. 7. The series of images from (a) to (f) shows the evolution of electrolyte damage as the small voids begin to cluster together to form large voids.

K-edge indicates that high electron dose induced damage causes lithium loss. This could be due to localized heating and/or by the electrostatic charging induced electric field which can drive away lithium in LIPON. It is important to note that LIPON has high lithium-ion conductivity at high temperatures.[26]

Figure 7 shows a series of bright field TEM images recorded at regular time intervals demonstrating the time evolution of damage in the LIPON electrolyte. Electrolyte damage is in the form of small voids which cluster to form a large void as shown by the low magnification image in Fig. 7(f). Similar bubble formation was observed during imaging in a scanning electron microscope operated at 10 kV with equal to or longer than $10\,\mu s$ dwell time. Such a bubble formation in LIPON is plausibly due to dissociation of N_2 at higher dose; this is typically referred as radiolysis. Radiolysis is predominant in polymers and ionic crystals such as NaCl with similar dose thresholds.[27] Consequently, imaging with SEM needs to be minimized during FIB fabrication processes to avoid electrolyte damage. Furthermore, LIPON electrolyte is highly sensitive to air/moisture specifically when its cross-sections are thinned down to 100 nm. Swollen electrolyte layer filled with voids was observed if the FIB prepared samples were not transferred to the TEM as soon

as possible (preferably less than 15 minutes). This highlights the importance of immediate transfer of nano-batteries from FIB to TEM for *in-situ* TEM biasing experiments.

4. Design of TEM/STEM Biasing Holders

The strict thinness requirements of TEM samples coupled with the need for electronic biasing of the solid-state batteries demand the creation of new TEM/STEM sample holder designs that fulfill these needs. These designs must accommodate the individual and separate electrical connections to the cathode and anode of the thin battery sample and the sample holder must have the electrical connections outside of the TEM where it could be connected to a potentiostat. Through exploratory work, a few experimental designs and new TEM holders have emerged and been tested. These designs include TEM holder designs from NanoFactory and ProtoChips, as both manufacturers produce TEM holders capable of electrically biasing the TEM sample.

The main components of successful electrical biasing of the TEM sample include the large TEM holder, sample carrier (where the TEM sample is mounted), and electrical connections from the sample to the sample carrier then finally to the outside end of the TEM holder. Many designs navigate through these obstacles with their own challenges. At the time of this writing, the NanoFactory designs have been used the most for experimentation. Firstly, a design which includes a thinned solid-state battery electrically connected to a sample carrier that serves as connectors to both the cathode and anode (separately of course) is used. The first design is illustrated in Fig. 8 for clarifications. The semi-circular gold coated pad is a custom-made pad from TEMwindows.com with about a 2.85 mm diameter and a 200 nm surface coating of SiN. The spacing between the two gold pads is 50 micron. The sample carrier is cut horizontally at the square window so that there will be easy access while working with FIB.

Secondly, a design in which the sample carrier makes one electrode connection and a piezo-controlled tip makes the second
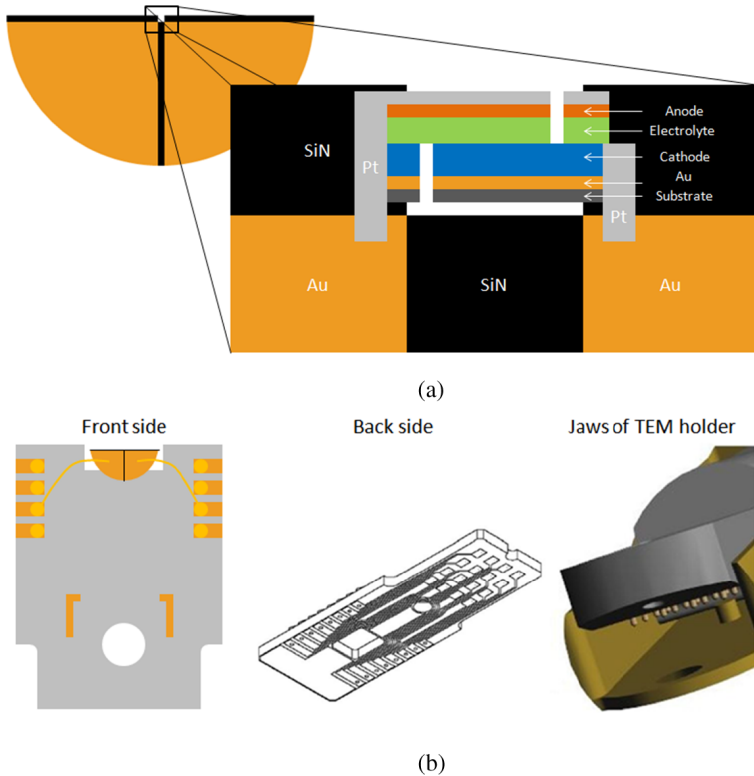
(a)

(b)

Fig. 8. First NanoFactory design with connections to both the cathode and anode. (a) The thin film battery sample is mounted on a SiN grid with two gold pads which is wired to the connections of the sample carrier. (b) The sample carrier is then loaded on to the TEM holder with jaws that make pin hold connections to the sample carrier. Figures courtesy of NanoFactory.

electrode connection is also explored. This design is illustrated in Fig. 9 for clarifications. The technical difficulties with this design lie with the piezo-controlled tip used for connection. When the TEM holder is placed within the TEM, the connection must be made with the tip using manual controls of the piezo-tip. Since the TEM beam will only provide a two-dimensional planar view of the solid-state battery, the depth information can only be obtained via trial and error. This process takes time and considerable skill to execute properly without physically damaging the solid-state battery. Models made by NanoFactory, such as the Multimodal
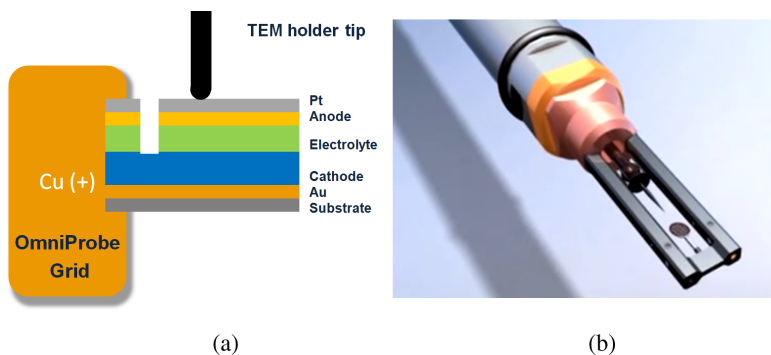
(a)   (b)

Fig. 9. (a) shows the electrical connection schematic of the nano-battery, (b) shows an overall view of the second NanoFactory design with connection to one electrode and a piezo-controlled connection to the second electrode. Courtesy of Brookhaven National Lab.

Optical NanoProbe, are suitable for electric biasing of solid-state thin battery in TEM column. One connection is made via the piezo-controlled tip and the second connection is simply made through the OmniProbe grid, which is conducting and is contacting the O-ring that holds it in place. The TEM holder itself will have leads connecting to the O-ring and piezo-controlled tip separately.

There are some advantages of one design over the other. The first design ensures contact to both electrodes, but the physical dimension of the SiN gap requires the nano-battery to be quite large, which can be difficult to work with using FIB. The second design is not limited by physical dimension restrictions, but the connection needs to be made in the TEM without a stereo view, which can be tricky due to lack of depth information.

In addition to the NanoFactory design, the ProtoChips Aduro TEM holder is also capable of electrically biasing TEM holders. Such designs have not been experimented with by our group but serve as potential alternatives. However, there are also other potential challenges that these TEM holder designs do not address. For example, the inability to protect the TEM sample from atmospheric conditions during sample carrier mounting on the TEM holder or sample transfer from FIB to TEM can be detrimental to lithium-ion battery electrode components that are sensitive to air moisture,
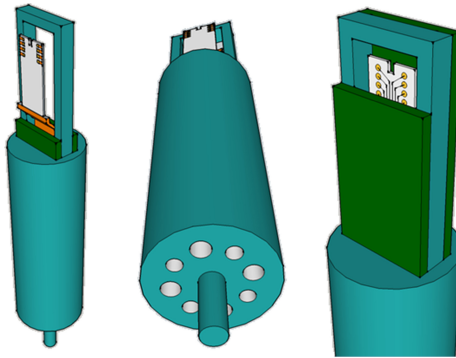
Fig. 10. Future designs of TEM holder with vacuum sealable capability for *in-situ* TEM as envisioned by the authors.

especially in the super thinned state. In our opinion, the next generation TEM holders for *in-situ* TEM will comprise of designs that eliminate the presence of air exposure conditions. A sample design by us is illustrated in Fig. 10.

The most important part of this design is a pair of closable doors on both sides of the frame that enclose the TEM sample carrier and keep the contents in vacuum. These doors (drawn with green parts) should be controlled remotely via radio frequency signals or similar technology, allowing opening and closing inside FIB or TEM to permit access. In the open door state, the sample carrier will be out of plane of the frame, allowing FIB interactions such as ion beam milling, Pt welding, and OmniProbe manipulations, which would be blocked by the frame top otherwise. While the doors are closing, the sample carrier will shift back in plane with the frame and allow full closure. Ideally, the sample carrier (white part) should be separable from the connection (orange part) for changing of the sample carriers. The sample carrier can allow multiple connections (eight connections denoted here) while it will be inserted into the orange connector. On the bottom side, there is a central rod that will fit into the slots of any standard modern SEM/FIB machines and other pin holes for the electrical connections. Once the samples are prepared and the vacuum doors closed, this TEM holder head can be connected to the rest of the TEM holder with an inverted part

that will make all the necessary connections with the TEM holder head. With the future physical fruition of this design, many new capabilities will be available for *in-situ* TEM experiments without the constraints of air exposure.

5. *In-situ* Analytical Characterization of Nano-Batteries using Imaging, Diffraction, and Spectroscopy

With the successful fabrication of functional solid-state nano-batteries using appropriate FIB fabrication parameters and careful electron-beam damage control under the TEM, many analytical characterization techniques can be conducted *in-situ* to observe the dynamics of lithiation processes in solid-state batteries. The foremost technique enabled is the *in-situ* TEM imaging of the nano-battery cross sections for *in-situ* morphological changes. In many battery chemistries, expansion of solid-state electrodes is of great importance to the performance of the battery. For example, amorphous silicon will expand in volume about 170% when lithiated to $\sim Li_{2.5}Si$ and over 280% when fully lithiated to $Li_{3.75}Si$,[28] causing stress in the electrode. Contrast changes in a two-phase interface propagating will provide kinetic rate information about the phase transformation. Additionally in certain solid-state battery setups, which include conversion electrodes such as FeF_2, significant morphological changes can also be observed.[2]

Electron diffraction also provides information for structural changes occurring in the electrodes during charging and discharge. Almost all electrodes will have some form of phase transformation during cycling that affects the performance of the cell. For instance, amorphous-crystalline interfaces present large interfacial strains within the electrodes, which could lead to pulverization and loss of capacity as in the case of silicon.[29–32]

More importantly, spectroscopic characterization, which provides chemical information, can be enabled with *in-situ* analytical TEM. Coupled with the spatial resolution of STEM mode, detailed analysis can be carried out *in situ*, mapping out the chemical concentration of elements of interest as lithiation progresses. The
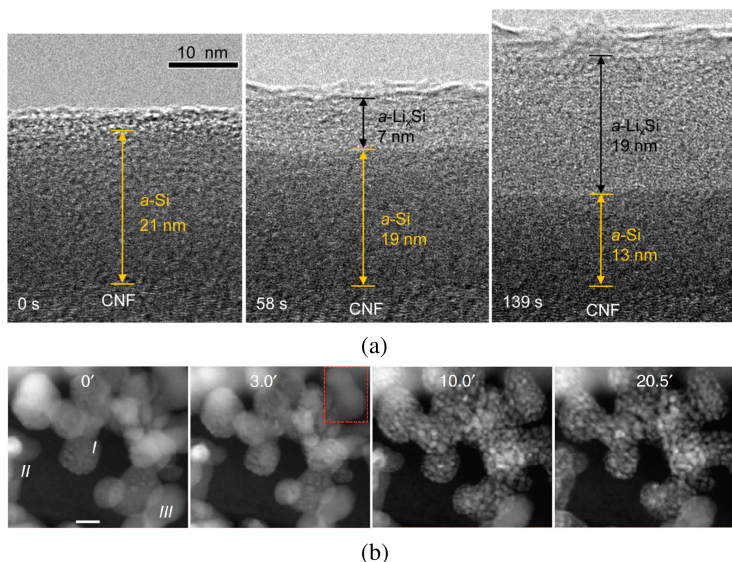
Fig. 11. (a) The series of images show the propagation of an a-Li$_x$Si phase into a-Si at a speed of about 0.06 nm/s.[28] (b) The series of images show the conversion reaction of FeF$_2$ particles into Fe nanoparticles imbedded in a LiF matrix.[2]

main technique providing such information is EELS included in many of today's modern TEMs.[33] It takes advantage of the difference in kinetic energy of the primary electrons after inelastic scatterings through the sample to identify the elemental composition of the material. When conducted in STEM mode of the TEM, EELS can couple nanometer-scale spatial resolution with elemental identification, providing a powerful technique that allows scientists to envision the lithium-ion transport movement across the solid electrolyte. Interesting phenomenon, such as interfacial accumulation, can be easily identified with EELS Li-K edge elemental mapping. Figure 12 demonstrates combined imaging and chemical analysis capability with high spatial resolution. The TEM sample is fabricated from a thin film solid-state battery consisting of SnO$_2$ (anode)/Li$_{3.4}$V$_{0.6}$Si$_{0.4}$O$_4$ (LVSO electrolyte)/LiNi$_{0.5}$Mn$_{1.5}$O$_4$ (cathode) deposited by pulsed laser deposition (PLD).[34] Lithium concentration mapping produced by EELS analysis will provide insight into the interfacial phenomena that are of high importance

TEM micrograph   **Ni, V, Li EELS map**   **Li intensity EELS map**
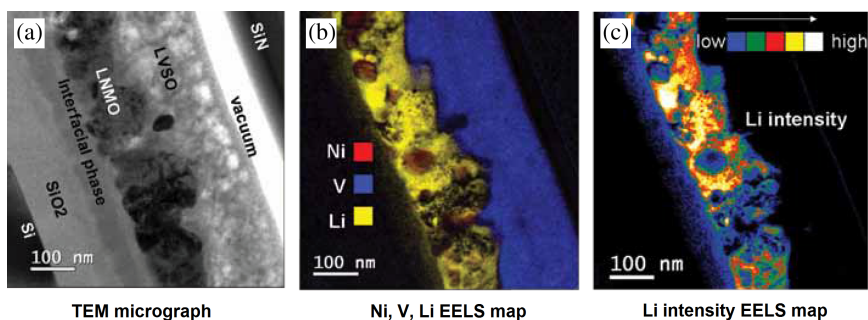
Fig. 12. (a) TEM image of the solid-state battery cross-section. (b) shows the respective elemental mappings of nickel, vanadium, and lithium. (c) shows the lithium concentration mapping using Li–K edge.[34]

in solid-state batteries. EELS is also capable of providing valuable oxidation state information of transition metal ions after careful analysis of fine structure peaks. For example, the L_3/L_2 peak ratio of Cobalt will be an indication of the oxidation state of Cobalt. Elemental Cobalt will have a L_3/L_2 peak ratio of about 3.77 whereas higher oxidation Cobalt will have a ratio of 2.90 at Co^{2+} and 2.43 at a mixture of Co^{3+} and Co^{2+}.[35]

An alternative to STEM/EELS is the energy filtered TEM. Conducted in the TEM mode, primary electrons passing through the sample are filtered by a magnetic prism to form contrast images formed by electrons of a specific energy. When the selected energy range is at the energy loss edge of a specific element, the resulting image shows a concentration map of the selected element.[36] The advantage of this technique is the absence of concentrated electron-beam compared to the focused probe of STEM mode; however, the image will only contain a limited energy range constraining the chemical information to one element at a time. It nevertheless will not carry the spectroscopic information that can be used to identify oxidation states as the intensities within the energy range are integrated together. Of course, each technique will present different information with its own advantages and disadvantages. Careful planning and preparation will allow the users to fully utilize these techniques available *in-situ* within the TEM.

With all the conditions properly managed, analytical electron microscopy of solid-state thin film batteries can be quite a powerful tool to analyze the interfacial phenomena present during the operation of thin film batteries. In a recent *ex-situ* STEM/EELS study,[17] the cathode/electrolyte and anode/electrolyte have both been shown to accumulate lithium. In the model system, the cell is constructed as lithium cobalt oxide, lithium phosphorus oxynitride, and amorphous silicon as cathode, electrolyte, and anode respectively. Upon overcharging of the anode to over three times its theoretical capacity to about $260\,\mu Ah/cm^2$, various additional interfaces form at the anode/electrolyte interface. Firstly, lithium plating occurs at the copper (current collector) and silicon interface to compensate for the extra capacity. Secondly, an inter-diffused interface of silicon and phosphorus forms, which could correspond to irreversible reactions between the anode and electrolyte. Detailed electron energy loss spectrums shown in Fig. 13 demonstrates the presence of lithium and phosphorus signals at position 0, while in the interface between silicon and LiPON, additional silicon signals are seen at position 1–2. In the silicon layer, lithium and silicon signals corresponds to the formation of lithiated silicon at position 3–4. Finally, from position 5–7, we only see lithium K-edge which is evidence for lithium plating.
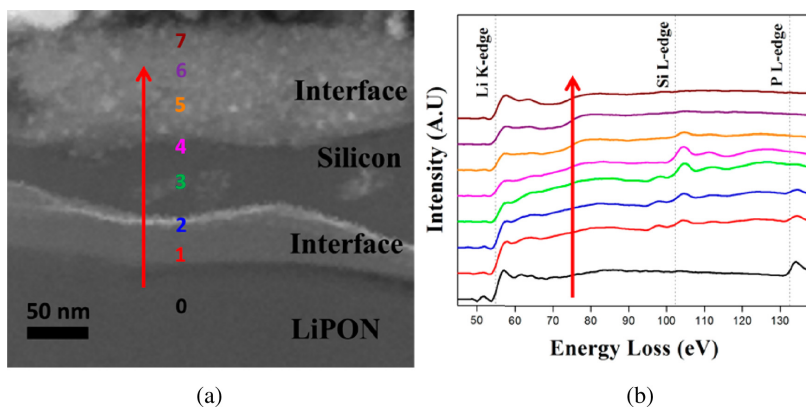

(a)   (b)

Fig. 13. (a) Annular Dark Field STEM image of the anode/electrolyte interface in a sample charged to $260\,\mu Ah/cm^2$. (b) Electron Energy Loss Spectra recorded from 8 different sites along the interface.[17]
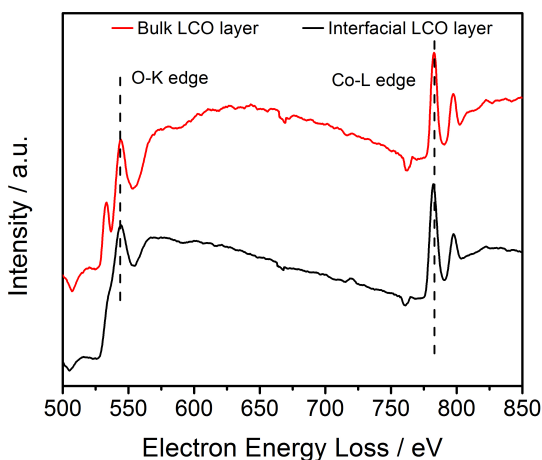
Fig. 14. (Color online) High loss EELS of the interfacial LCO layer (black) and bulk LCO layer (red). The O–K pre-edge is severely diminished in the interfacial LCO layer indicating Co-O bonding and coordination changes.

With further study, the cathode/electrolyte interface showed a short range ordered lithium cobalt oxide layer between LiPON and bulk lithium cobalt oxide that accumulated lithium along with chemical bonding changes upon charging. Upon charging, *ex-situ* EELS analysis showed O–K pre-edge disappearance (Fig. 14) in this interfacial layer indicating oxygen vacancy formation as the O–K pre-edge is heavily influenced by the bonding between transition metal ion and oxygen. O–K edge electron energy loss spectrum probes unoccupied 2p orbitals of oxygen. Since the transition metal 3d electrons are hybridized with the oxygen 2p electrons, analysis of the edge along with the pre-edge provide information about energy splitting and type of coordination of the transition metal including presence of oxygen vacancies.[37] Li–K edge concentration mappings also show lithium accumulation within this layer contributing to possible capacity loss. Interestingly, our recent *in-situ* EELS analysis only shows a shifting of O–K pre-edge suggesting oxygen vacancy formation is not kinetically favored.[38] These findings demonstrate the unique analytical information STEM/EELS characterization can provide with high spatial resolution and chemical sensitivity.

More importantly, the difference between *in-situ* and *ex-situ* analysis clearly points to the dynamic information that can be lost in *ex-situ* experiments.

6. Future Perspectives — Opportunities and Challenges

Once the *in-situ* analytical electron microscopy of solid-state batteries technique matures with further studies, many experimental opportunities are open for analysis of different interfacial phenomena that are not present in other types of systems such as nanowires and nanoparticles. The most immediate progression is the introduction of different chemistries for electrodes and/or electrolytes. Other types of intercalation materials such as $LiNi_{0.5}Mn_{1.5}O_4$ high voltage spinel, and lithium excess layered material are of interest as they have unique structural and chemical changes during electrochemical operations. For example, lithium excess material has been shown to undergo surface transition from layered structure to spinel structure with transition metal migration.[39] With a solid-state battery configuration, this surface phase transformation could be monitored by *in-situ* TEM to obtain dynamic information of the transition metal migration. Different types of electrolytes could be explored, such as the recently discovered LLZO (Garnet) and LLTO (Perovskite) structures. Their interfaces with the electrode materials remain largely unknown at the time this chapter was written.

Future experiments will also include observations with high temporal resolution. *In-situ* EELS mapping could help visualize the lithium concentration during charging and demonstrate lithium transport at the interfaces in real time. Morphological and structural changes are very important with conversion materials and the solid-state battery setup will provide a closer representation of electrode operation in a full cell rather than just the material itself. Dynamic transition metal and anion bonding changes can be monitored by *in-situ* high loss EELS through the bulk of the electrode with high spatial resolution. Changes in the O–K edge will reflect changes in the transition metal and oxygen bonding, while transition metal L_3/L_2 edge ratios will reflect its oxidation state. All these characterizations provide a wide range of information about

the mechanism and dynamics of chemical changes in the electrode in a full cell environment.

However, the community will face many fabrication and technical challenges to enable *in-situ* STEM/EELS characterization with high temporal resolution. With more frequent e-beam scanning, there is a higher dosage of electrons on the sample. Selecting solid-state electrolytes that can withstand such intense beam exposure is of vital importance to push the limits of *in-situ* STEM/EELS analysis. Certain Garnet type, Perovskite type, and amorphous materials could function as electrolytes that survive higher doses of electron beam without decomposition. Additionally, the biasing current is still too high for lower charge/discharge rate experiments. Even at the pico-ampere range, the current density is still on the orders of $100\,\mu A/cm^2$ which corresponds to about 1C (one hour charge/discharge). Near-equilibrium reactions will require slower rates; hence femto-ampere potentiostats will be needed to bias the samples given their nano-sized area. A second strategy is to use Dynamic TEM for the characterization of solid-state batteries. This technique has been under intense development in recent years, though typically used in biological beam-sensitive samples. Nanosecond time-scale Dynamic TEM requires high intensity electron beams in a short nanosecond pulse, and Dynamic TEM achieves such requirements by introducing laser stimulated photoemission electron source to generate excess of 2×10^9 photo-emitted electrons in a single 15-ns bunch. Such capabilities enable observation of transient morphological and diffraction changes with high temporal resolution that can be missed in conventional TEM.[40–43] We expect that the battery community will greatly benefit from the advancement in DTEM. In summary, high temporal resolution STEM/EELS characterization will provide critical new insights of dynamic interfacial phenomena that would shed light on the design and optimization of future solid-state batteries, a safer and more reliable energy storage technology.

Acknowledgments

References

1. X. H. Liu *et al.*, *Nano Lett.* **11** (2011) 3312–3318.
2. F. Wang *et al.*, *Nat. Commun.* **3** (2012) 1201.
3. X. H. Liu *et al.*, *Nano Lett.* **11** (2011) 3991–3997.
4. L. Q. Zhang *et al.*, *ACS Nano* **6** (2011) 4800–4809.
5. K. Yamamoto *et al.*, *Angew. Chem. Int. Ed.* **49** (2010) 4414–4417.
6. X. H. Liu *et al.*, *Nano Lett.* **11** (2011) 2251–2258.
7. J. Y. Huang *et al.*, *Science* **330** (2010) 1515–1520.
8. C. M. Wang *et al.*, *Nano Lett.* **11** (2011) 1874–1880.
9. L. A. Giannuzi and F. A. Stevie. *Introduction to Focused Ion Beams: Instrumentation, Theory, Techniques and Practice*, (Springer, New York, 2005).
10. J. Mayer, L. A. Giannuzi, T. Kamino and J. Michael, *MRS Bull.* **32** (2007) 400–407.
11. A. Lugstein, B. Basnar and E. Bertagnolli, *J. Vac. Sci. Technol. B.* **20** (2002) 2238–2242.
12. S. Rubanov and P. R. Munroe, *J. Mater. Sci. Lett.* **20** (2001) 1181–1183.
13. N. I. Kato, *J. Elect. Micro.* **53** (2004) 451–458.
14. S. Bals, W. Tirry, R. Geurts, Z. Yang and D. Schryvers, *Microsc. Microanal.* **13** (2007) 80–86.
15. N. Miyajima *et al.*, *J. Elect. Microsc.* **238** (2010) 200–209.
16. M. Scahaffer, B. Schaffer and Q. Ramasse, *Ultramicroscopy* **114** (2012) 62–71.
17. D. Santhanagopalan *et al.*, *J. Phys. Chem. Lett.* (2013) 298–303.
18. N. Balke *et al.*, *Nano Lett.* **10** (2010) 3420–3425.
19. R. F. Egerton, P. Li and M. Malac, *Micron* **35** (2004) 399–409.
20. J. P. Buban, Q. Ramasse, B. Gipson, N. D. Browning and H. Stahlberg, *J. Elect. Microsc.* **59** (2010) 103–112.
21. E. G. Rightor *et al.*, *J. Phys. Chem. B.* **101** (1997) 1950–1960.
22. N. Jiang and J. C. H. Spence, *Ultramicroscopy* **113** (2012) 77–82.
23. P. Li and R. F. Egerton, *Ultramicroscopy* **101** (2004) 161–172.
24. J. B. Bates *et al.*, *Sol. Stat. Ionics.* **53–56** (1992) 647–654.
25. X. Yu, J. B. Bates, G. E. Jellison J. and F. X. Hart, *J. Electrochem. Soc.* **144** (1997) 524–532.
26. X. Yu, J. B. Bates and G. E. J. Jellison, *188th Meeting of the Electrochemical Society*, Vol. 95, ed. J. B. Bates, (Electrochemical Society, Pennington, New Jersey, Chicago, Illinois, 1996).
27. R. F. Egerton, *Microsc. Res. Techniq.* **75** (2012) 1550–1556.

28. J. W. Wang *et al.*, *Nano Lett.* (2013) 709–715.
29. X. H. Liu *et al.*, *ACS Nano* **6** (2012) 1522–1531.
30. S. W. Lee, M. T. McDowell, L. A. Berla, W. D. Nix and Y. Cui, *Proc. Natl. Acad. Sci. U. S. A.* **109** (2012) 4080.
31. K. J. Zhao *et al.*, *J. Electrochem. Soc.* **159** (2012) A238.
32. J. W. Wang *et al.*, *Nano Lett.* **13** (2013) 709–715.
33. R. F. Egerton, *Reports on Progress in Physics* **72** (2009) 016502.
34. Y. S. Meng *et al.*, *Elec .Chem. Soc. Interface.* **20** (2011) 49–53.
35. B. D. Yuhas, D. O. Zitoun, P. J. Pauzauskie, R. He and P. Yang, *Angewandte Chemie* **118** (2006) 434–437.
36. P. A. Midgley and M. Weyland, *Ultramicroscopy* **96** (2003) 413–431.
37. J. Graetz *et al.*, *J. Phys. Chem. B* **106** (2002) 1286–1289.
38. Z. Wang *et al.*, Manuscript in Preparation. (2014).
39. B. Xu, C. R. Fell, M. Chi and Y. S. Meng, *Energy and Environmental Science* **4** (2011) 2223–2233.
40. J. S. Kim *et al.*, *Science* **321** (2008).
41. J. E. Evans, K. L. Jungjohann, N. D. Browning and I. Arslan, *Nano Lett.* **11** (2011) 2809–2813.
42. M. R. Armstrong *et al.*, *Ultramicroscopy* **107** (2007) 356–367.
43. T. LaGrange *et al.*, *Ultramicroscopy* **108** (2008) 1441–1449.